



# Optimization of Hull Thin Plate Welding Sequence Based on Simulated Annealing-Back Propagation Neural Network

Hao Xu<sup>1\*</sup>, Daofang Chang<sup>2</sup>, Chiyike Zhang<sup>3</sup>

<sup>1</sup> Logistics Science and Engineering Research Institute, Shanghai Maritime University, 201306 Shanghai, China

<sup>2</sup> Logistics Engineering College, Shanghai Maritime University, 201306 Shanghai, China

<sup>3</sup> Jiangnan Shipyard Group Co., Ltd, 201306 Shanghai, China

\* Correspondence: Hao Xu (202230510268@stu.shmtu.edu.cn)

Received: 11-25-2024

Revised: 01-08-2025

Accepted: 01-14-2025

**Citation:** H. Xu, D. F. Chang, and C. Y. K. Zhang, "Optimization of hull thin plate welding sequence based on Simulated Annealing-Back Propagation neural network," *Precis. Mech. Digit. Fabr.*, vol. 2, no. 1, pp. 1–11, 2025. <https://doi.org/10.56578/pmdf020101>.



© 2025 by the author(s). Licensee Acadlore Publishing Services Limited, Hong Kong. This article can be downloaded for free, and reused and quoted with a citation of the original published version, under the CC BY 4.0 license.

**Abstract:** In the ship hull plate welding process, different welding sequences directly affect the deformation of the current welding procedure, which in turn impacts the overall shipbuilding accuracy. This study takes a typical double T-shaped thin plate structure as an example. Based on welding numerical simulation and experimental validation, a corresponding dataset is obtained. To address the issue of BP neural networks being prone to local optima, which can lead to inaccurate results, a Simulated Annealing-Back Propagation (SA-BP) neural network model is used to analyze the dataset. The research aims to determine the optimal welding sequence that minimizes deformation. The training results show that the Mean Squared Error (MSE) of the SA-BP model decreased from 1.0144 in the BP model to 0.67388. Additionally, the SA-BP model's fitting performance is far superior to that of the BP model. Therefore, the SA-BP neural network model provides more stable and accurate results compared to the traditional BP neural network model. The comparison of the optimal welding sequence results derived from both models shows that welding with the optimized SA-BP neural network results in a 21.07% reduction in welding deformation compared to the traditional BP neural network.

**Keywords:** Welding deformation; Hull thin plate; Simulated Annealing (SA) algorithm; Simulated Annealing-Back Propagation (SA-BP) neural network

## 1 Introduction

Currently, 30%–40% of the labor time in shipbuilding is occupied by welding operations, and the cost of welding accounts for more than 30% of the total cost. At the same time, the welding process is complex and irreversible. Welding deformation directly affects product quality, structural strength, and subsequent assembly processes. Over the years, many scholars have used finite element analysis numerical simulation methods to predict welding deformation and study processes that control residual stress, reduce welding deformation, and improve welding quality [1, 2]. Chen and Soares [3] performed numerical simulation analysis of the welding process based on longitudinal rib forced alignment using a sequentially coupled thermo-elastoplastic finite element method, and studied the impact of longitudinal rib misalignment on welding deformation and stress. Ghafouri et al. [4] used a combination of experimental and numerical simulation methods to predict the welding deformation of ultra-high-strength steel complex thin-walled structures, and based on the calculation results, they clarified the mechanism of the effect of forced restraint on the welding deformation of this structure. Lu et al. [5] developed an efficient enhanced moving heat source model based on the general finite element software platform named MSC. Marc, and used the thermo-elastoplastic finite element method and the enhanced moving heat source model to perform numerical simulations of the welding deformation of a large long straight structure (13,832 mm in length) of a locomotive vehicle, while verifying that welding sequence has a significant effect on both the mode and magnitude of welding deformation. Zhao et al. [6] used a combination of experimental and simulation methods to comparatively analyze the effect of two different welding sequences and four different directions on the residual stress of X80 pipeline steel during multi-layer, multi-pass welding. Azad et al. [7] used the thermo-elastoplastic analysis method of ABAQUS finite element software to analyze the residual stress and residual deformation of the welded joint of 32 mm thick Q345qD steel under gas metal arc

welding, and combined experimental tests and numerical simulation to study the effect of four different welding sequences on the residual stress distribution and residual deformation of the welded joint.

When studying the effects of different welding sequences on welded parts, a commonly used method is to select individual sequences [8, 9] and perform comparisons through finite element simulation. However, when there are many welding sequences and the situation is complex, comparing only a few sequences cannot determine the optimal welding sequence. Therefore, this study uses a combination of welding numerical simulation and neural networks. It uses simulation software to simulate the deformation during the welding process and form a dataset. Through data analysis, it determines the optimal welding sequence that minimizes deformation, which is suitable for various complex welding situations.

## 2 Thin Plate Finite Element Model Establishment

### 2.1 Geometric Model Establishment and Mesh Division

In shipbuilding, plates with a thickness of less than 6 mm are generally classified as thin plates [10]. Thin plate structures are mainly used for the deck and some external plates of the ship's superstructure, which reduces the ship's center of gravity and lightens the overall weight, thereby significantly improving the performance of the hull [11]. However, due to the smaller thickness of thin plates, they are more prone to instability and deformation during welding, as a result of uneven heating and local plastic strain [12]. Compared to thicker plates, thin plates are more susceptible to instability and deformation, which greatly affects the ship's structural performance, strength, toughness, aesthetics, and precision control, severely impacting overall construction quality [13]. During the plate welding process, when there are multiple welding modules, the welding sequence directly affects the deformation of the plate. However, due to the large number of possible welding sequence combinations, conducting individual sequence trials in production would incur huge production and time costs [14]. Therefore, numerical simulation calculations of welding are required. Considering the time required for numerical simulation, this study uses the results of the simulations and adopts an SA-BP neural network model for training to ultimately determine the optimal welding sequence.

The double T-shaped thin plate structure, as a common structure in the hull welding process [15], is selected as the model for this study. The finite element model is geometrically modeled using software. The model consists of one panel and two web plates, with dimensions of 800 mm × 600 mm × 4 mm for the panel, and 800 mm × 100 mm × 4 mm for the two web plates. In geometric modeling, mesh division is crucial because it significantly affects modeling accuracy and computational time. To improve computational efficiency while ensuring accuracy, fine mesh is used in the welding area, and the mesh gradually coarsens away from the welding area. The structural model of the double T-shaped thin plate is shown in Figure 1.

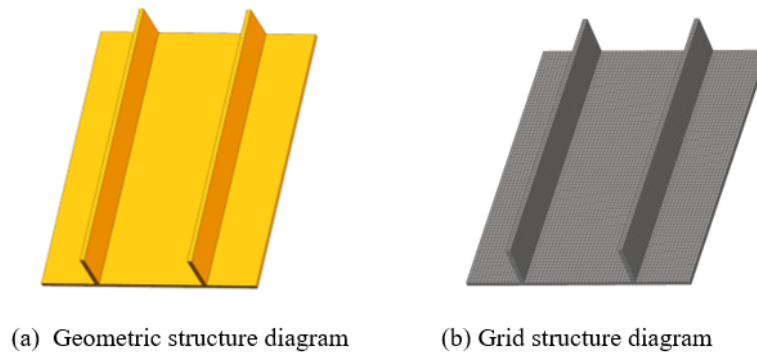


**Figure 1.** Double T-shaped thin plate structure

### 2.2 Welding Heat Source Model Establishment

The welding heat source model is a mathematical representation that describes the time and spatial distribution of heat input applied to the workpiece during welding. It forms the basis for welding numerical simulation. This study focuses on thin plate welding, where the heat flow not only acts on the surface of the workpiece but also distributes along the thickness direction, with the heat source being a volumetric distribution. Since the welding method is arc welding, the shape of the heat source, according to relevant literature [16, 17], is a double ellipsoidal shape with asymmetric front and rear ends. This heat source model considers the temperature gradient at the front and rear ends of the welding heat source center, as well as the distribution characteristics along the plate thickness direction, allowing for an accurate simulation of the heat input in arc welding. Therefore, the double ellipsoidal heat source model proposed by Goldak et al. [18] is selected for the welding simulation in this chapter, and its expression is as follows:

$$q_f(x, y, z) = \frac{6\sqrt{3}f_f\eta Q}{a_f b c \pi \sqrt{\pi}} \exp\left(-\frac{3x^2}{a_f^2} - \frac{3y^2}{b^2} - \frac{3z^2}{c^2}\right) \quad (1)$$

$$q_r(x, y, z) = \frac{6\sqrt{3}f_r\eta Q}{a_r b c \pi \sqrt{\pi}} \exp\left(-\frac{3x^2}{a_r^2} - \frac{3y^2}{b^2} - \frac{3z^2}{c^2}\right) \quad (2)$$

where,

$$x = (x - x_0 - vt) \quad (3)$$

$$y = (y - y_0) \cos \theta + (z - z_0) \sin \theta \quad (4)$$

$$z = (y - y_0) \sin \theta + (z - z_0) \cos \theta \quad (5)$$

In these equations:  $(x_0, y_0, z_0)$  represents the position of the heat source in the coordinate system  $(x, y, z)$ ;  $Q$  is the heat input;  $\eta$  is the heat efficiency, taken as 0.85;  $v$  is the welding speed;  $t$  is the instantaneous time of welding;  $a_f$  and  $a_r$  represent the semi-axes lengths of the ellipsoid at the front and rear, respectively;  $b$  represents the width of the ellipsoid;  $c$  represents the depth of the ellipsoid;  $f_f$  and  $f_r$  are the energy distribution coefficients at the front and rear of the double ellipsoid heat source. The double ellipsoidal heat source model is shown in Figure 2, with basic parameters: front semi-axis length  $a_f = 1.5$  mm, rear semi-axis length  $a_r = 6.0$  mm, width  $b = 3.7$  mm, depth  $d = 4.0$  mm.

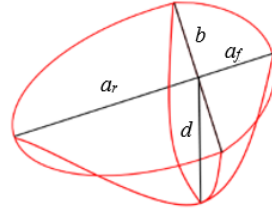


**Figure 2.** Double ellipsoidal heat source model

### 2.3 Thermodynamic Parameters of Welding Materials

AH36 high-strength steel is a low-alloy high-strength structural steel [19], known for its high rigidity, high strength, and good impact resistance. It is commonly used in shipbuilding. Arc welding of AH36 steel may cause issues such as low welding efficiency, large welding deformation, and high residual stress. The mechanical properties of AH36 steel follow the linear kinematic hardening criterion and the Von Mises yield criterion [20]. The physical and mechanical properties of AH36 steel, including thermal conductivity, density, specific heat, thermal expansion coefficient, Young's modulus, and yield strength variations with temperature, are shown in Figure 3. The Poisson's ratio of this material is 0.28 [21].

## 3 Finite Element Simulation Data and Experimental Verification

### 3.1 Finite Element Simulation

The thin plate welding in this study is multi-pass welding. In actual working conditions, if the weld pass is too long, it will be segmented. Taking this double T-shaped thin plate as an example, the welds at the junctions of each web plate and the panel are divided into two equal-length segments, totaling 8 weld passes. The welding sequence is unified as bottom to top, without considering reverse welding. For ease of data generation, these 8 weld passes are numbered in sequence. The specific labeling is shown in Figure 4.

In the case of a unified welding direction, there are as many as 8 possible welding pass sequences. Simulating all these results through numerical methods and finding the optimal welding sequence would consume a considerable amount of time. If only a few specific sequences are selected for comparison, the results may not accurately identify the optimal welding sequence. Therefore, this study proposes an approach to simulate a subset of welding sequences using professional welding simulation software, Simufact.Welding [22]. The welding sequence and corresponding

deformation values are used as a dataset, and the accuracy of the data is verified through experiments. Finally, data analysis is employed to decide the optimal welding sequence.

Therefore, 500 random sequences of this workpiece are selected for finite element simulation, and the deformation variation over time is shown in Figure 5. To standardize the welding deformation at different time points, the maximum deformation point during the entire welding process is taken as the deformation parameter for each welding sequence. The 500 welding sequences and their corresponding deformation parameters are compiled into a dataset, which serves as the basis for the subsequent decision-making regarding the optimal welding sequence.

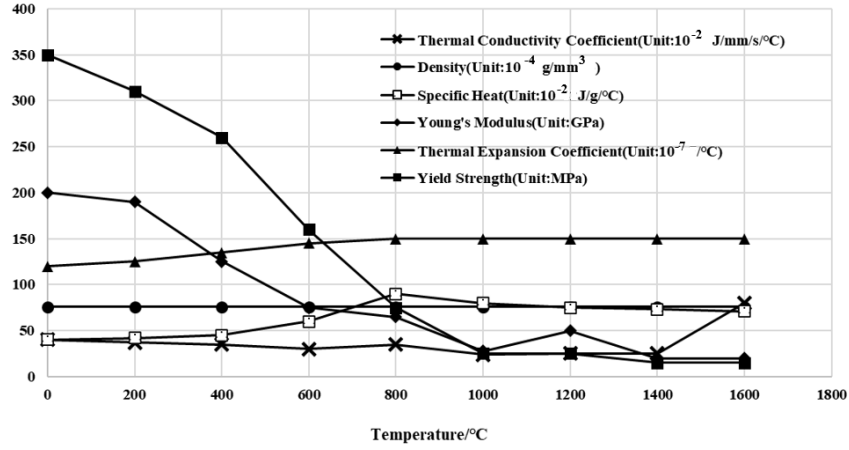


Figure 3. AH36 material properties

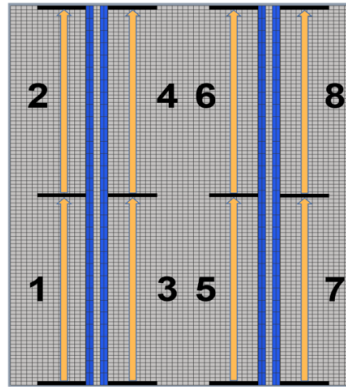


Figure 4. Welding direction and sequence

### 3.2 Experimental Verification

To verify the accuracy of the data obtained from the simulation, the results of the simulated deformation are compared with the actual deformation of the plate in the experimental verification.

This experiment was conducted in collaboration with a metal processing company, where an AH36 steel plate was precisely processed. A panel of 800mm×600mm×4mm and two web plates of 800mm×100mm×4mm were cut for actual welding, as shown in Figure 6. To ensure the accuracy of the experiment, the materials, specifications, and integrity of the cut panel and web plates were kept consistent with the materials used in the numerical simulation experiment, without considering the changes in physical properties caused by the cutting process.

The same arc welding process used in the simulation experiment was applied to weld the plates. During the experiment, controllable parameters such as welding speed, direction, and time were kept consistent with the simulation environment. As a reference experiment, the welding sequence 1-2-3-4-5-6-7-8 was used, and the welded double T-shaped thin plate is shown in Figure 7.

From the simulation experiment, we know that under this welding sequence, the maximum deformation of the plate is 2.36 cm. After observing the actual welded double T-shaped plate, visible deformation was noticed. To ensure the accuracy of the experiment, a laser distance meter was used to measure the deformation of the plate, which was found to be 2.33 cm. The error was 0.03 cm, only 1.27% of the simulated value, which is within the experimental

error range. The experiment proves that the data obtained from the simulation are real and valid and can be used as data support.

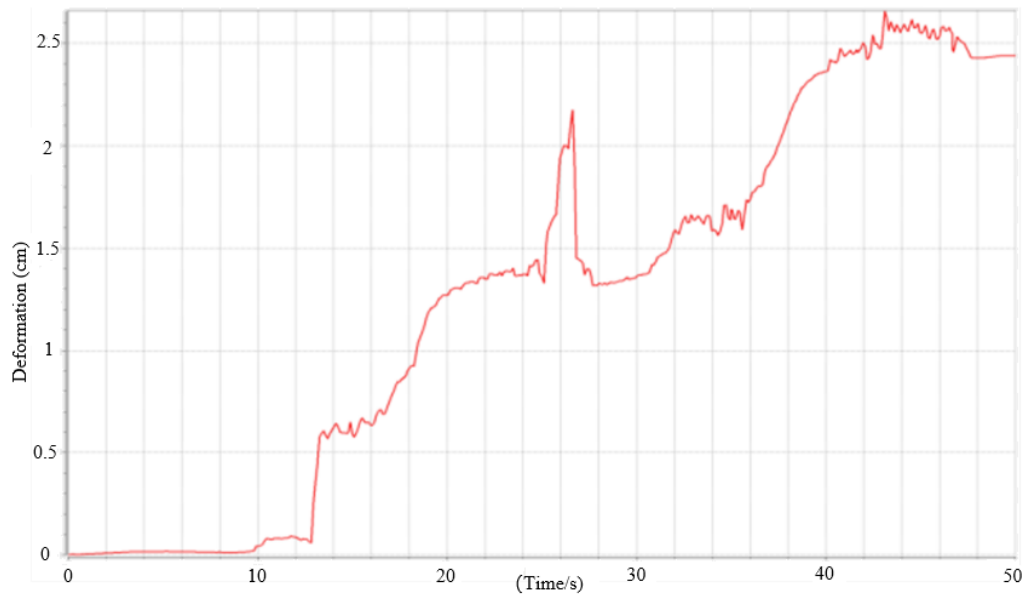
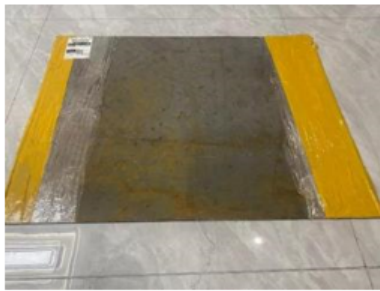


**Figure 5.** Variable variation over time



(a) Style diagram of double T-shaped structural panel



(b) Double T-shaped structural web style diagram

**Figure 6.** Style diagram of double T-shaped thin plate structure



(a) Top view of welded parts



(b) Front view of welded parts

**Figure 7.** Welding component view

## 4 SA Optimized BP Neural Network

To optimize the weights of the BP neural network, accelerate the convergence speed, and avoid getting trapped in local optima, this study uses a SA algorithm to optimize the BP neural network for welding sequence optimization [23]. The network is trained on different deformation values caused by various welding sequences to obtain the optimal welding sequence and results.

### 4.1 BP Neural Network Establishment

#### 4.1.1 BP neural network modeling

Figure 8 shows a typical three-layer BP neural network composed of the input layer, hidden layer, and output layer [24].

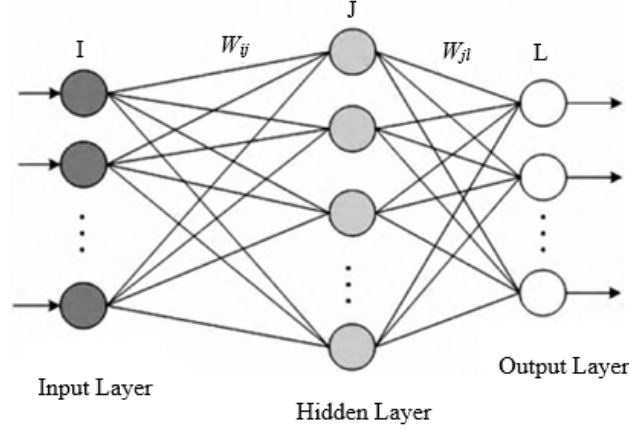


**Figure 8.** Typical three-layer BP neural network

$W_{ij}$  represents the weight vector from the input layer to the hidden layer, and  $W_{jl}$  represents the weight vector from the hidden layer to the output layer. The activation function for each node in the network layers is set to the commonly used ReLU (Rectified Linear Unit) function:

$$f(x) = \begin{cases} x, & x > 0 \\ 0, & x < 0 \end{cases} \quad (6)$$

The input, hidden, and output layers are denoted by uppercase letters  $I$ ,  $J$ , and  $L$ , respectively, with subscripts in and out denoting input and output, and subscripts  $i$ ,  $j$ , and  $l$  referring to the  $i$ -th,  $j$ -th, and  $l$ -th node in the respective layers.

The inputs and outputs for each layer are given by:

$$J_j^{in} = \sum_i W_{ij} I_i^{out} \quad (7)$$

$$J_j^{out} = f(J_j^{in}) \quad (8)$$

$$L_l^{in} = \sum_j W_{jl} J_j^{out} \quad (9)$$

$$L_l^{out} = f(L_l^{in}) \quad (10)$$

The error of the network is defined as the difference between the training output and the expected output, given by  $e = L_l^{out} - L_l^r$ . If the output layer has  $n$  nodes, the squared error between the training output and the expected output is:

$$E = \frac{1}{2} \sum_{l=1}^n (L_l^{out} - L_l^r)^2 \quad (11)$$

where,  $L_l^r$  is the expected output for the sample point.



#### 4.1.2 Determining the number of neurons

The eight digits representing welding sequences are used as the input layer for the neural network, and the corresponding deformation values are used as the output layer. Therefore, the number of neurons in the input layer is 8, and the number of neurons in the output layer is 1. The number of neurons in the hidden layer is determined using the following empirical formula [25]:

$$m = \sqrt{n + l} + a \quad (12)$$

where,  $m$  is the number of neurons in the hidden layer,  $n$  is the number of neurons in the input layer,  $l$  is the number of neurons in the output layer, and  $a$  is a constant between 1 and 10. Therefore, the number of neurons in the hidden layer is set to 10.

#### 4.2 SA Optimized BP Neural Network Algorithm Design

The SA algorithm simulates the process of solid annealing, including three stages: heating, isothermal, and cooling. During the isothermal stage, the SA algorithm accepts worse solutions with a certain probability, helping it avoid local optima and ultimately find the global optimum. In this study, Simulated Annealing is used to optimize the weights of the neural network, preventing the BP neural network from getting trapped in local minima and achieving optimization. The main steps of the algorithm are as follows:

##### Step 1: Algorithm Initialization

Set the initial temperature  $T_0$ , the length of the Markov chain  $L$ , construct the BP neural network, and randomly initialize the neural network weights to get the initial solution vector  $S_0$ .

##### Step 2: Perturbation

$$f(k+1) = f(k) + \eta\xi \quad (13)$$

where,  $\eta$  is the perturbation magnitude and  $\xi$  is a random disturbance variable.

##### Step 3: Compute the Increment

Calculate the increment  $dE = E(S_{k+1}) - E(S_k)$  of  $S_{k+1}$ , where  $E(S_k)$  is the squared error corresponding to  $S_k$ .

##### Step 4: Metropolis Acceptance Criterion

Using the Metropolis criterion, decide whether to accept the new solution. If  $dE < 0$ , the new solution is accepted with probability 1. Otherwise, a uniform random number  $\varepsilon$  is generated in the interval  $[0,1]$ . If  $\varepsilon < P$ , the new solution is accepted; otherwise, it is rejected and the process moves to the next step:

$$P = \begin{cases} 1, & E(k+1) < E(k) \\ e^{-\frac{E(k+1) - E(k)}{T}}, & E(k+1) \geq E(k) \end{cases} \quad (14)$$

##### Step 5: Inner Loop Termination Criterion

The termination condition for the inner loop is chosen as a time-consistent simulation. This means the temperature's Markov chain length  $L$  is fully traversed before performing the cooling operation.

##### Step 6: Cooling

The cooling operation is carried out using the commonly applied temperature decay function shown below:

$$T_{k+1} = \alpha T_k (k = 0, 1, 2, 3 \dots) \quad (15)$$

where,  $T_k$  is the temperature after  $K$  iterations,  $T_{k+1}$  is the temperature after one cooling step, and  $\alpha \in (0.5, 0.99)$  is any constant.

##### Step 7: Outer Loop Termination Criterion

The outer loop termination criterion is controlled by the total number of iterations. The algorithm ends when the total number of iterations reaches the preset limit. Otherwise, the process returns to Step 2. The final flowchart of the SA-optimized BP neural network algorithm is shown in Figure 9 [26].

#### 4.3 Verification and Analysis

Through physical experiments, the reliability of the numerical simulations and the accuracy of the data have been verified. To validate the SA-BP neural network model for welding sequence optimization proposed in this study, the dataset obtained from previous simulations was selected as a sample for algorithm verification. The optimal welding sequence was determined, and the corresponding dataset was generated. Some of the data is shown in Table 1.

##### (1) Traditional BP Neural Network Prediction of the Optimal Welding Sequence

When the unoptimized traditional BP neural network model was used for data prediction and analysis, the optimal welding sequence obtained was [1 7 3 5 4 6 8 2], with a corresponding deformation value of 1.50427.

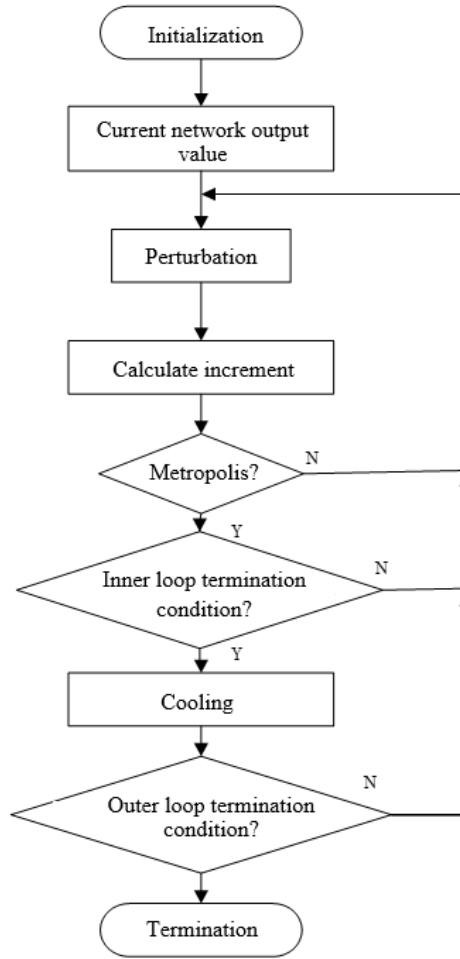


**Figure 9.** SA-BP neural network algorithm flowchart

**Table 1.** Partial data examples

Weld Bead 1	Weld Bead 2	Weld Bead 3	Weld Bead 4	Weld Bead 5	Weld Bead 6	Weld Bead 7	Weld Bead 8	Type Variable
1	2	3	4	5	6	7	8	2.73
8	1	3	5	2	7	4	6	1.07
6	5	3	1	8	2	7	4	2.89
8	4	5	1	6	2	7	3	3.85
3	6	2	4	5	1	8	7	2.01
3	8	4	7	1	5	6	2	1.47
7	6	3	4	2	5	1	8	3.95

The Mean Squared Error (MSE) was 0.00239 (rounded to five decimal places).

## (2) SA-BP Neural Network Prediction of the Optimal Welding Sequence

When the optimized SA-BP neural network model was used for data prediction and analysis, the optimal welding sequence obtained was [1 7 8 6 3 4 2 5], with a corresponding deformation value of 1.18726.

The MSE was 0.00143 (rounded to five decimal places).

In Figure 10, the x-axis represents the number of network iterations, and the y-axis represents the training MSE. The dashed line represents the preset error goal, while the solid line shows how the error changes with each iteration. From subgraphs (a) and (b) of Figure 10, it can be seen that the traditional BP model reaches the optimal solution after 9 iterations, with an MSE of 1.0144. Clearly, the network gets stuck in a local optimum. In contrast, the SA-BP model reaches the optimal solution after the 4th iteration, with an MSE of 0.67388, which is much lower than that of the traditional BP neural network. Under the same training conditions, the MSE of the SA-BP model is lower than that of the BP neural network. Furthermore, from the fitting effect subgraphs (c) and (d) of Figure 10, it is evident that the SA-BP model provides better fitting results than the traditional BP neural network. Thus, it can be concluded



that the SA-BP model is more likely to reach a global optimum and that the quality of the SA-BP model is better, offering more accurate predictions.

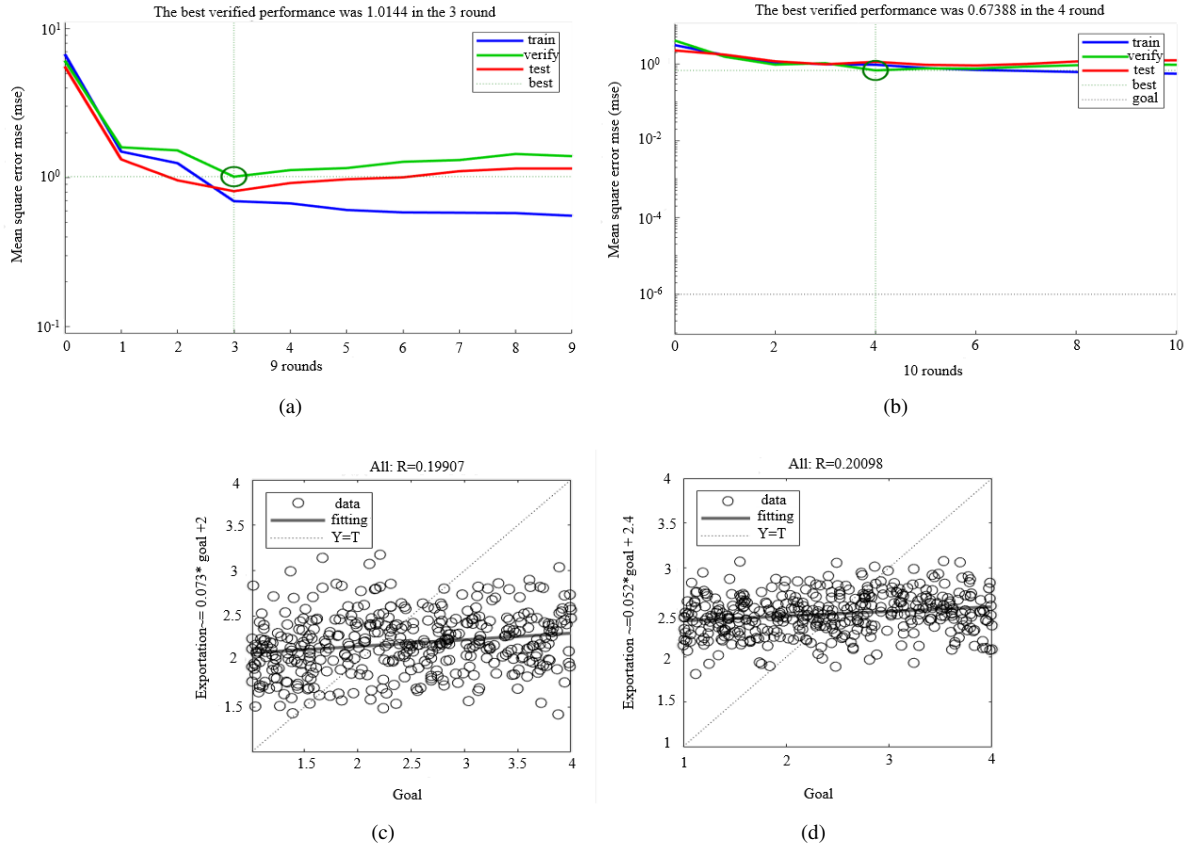


**Figure 10.** Model training situation: (a) Traditional BP neural network training process; (b) Training process of SA-BP neural network; (c) The fitting effect of traditional BP neural network; (d) SA-BP neural network fitting effect

## 5 Conclusions

Taking the double-T thin plate as the research object, the SA-BP neural network model was used to analyze the collected data, determining the optimal welding sequence and the corresponding deformation values.

(1) To address the issue that welding sequence affects the plate deformation and, consequently, the shipbuilding accuracy, this study proposes a method combining welding numerical simulation with the SA-BP neural network. The proposed algorithm has the advantages of low computational cost and simplicity, and by optimizing the weights of the BP neural network using the SA algorithm, it avoids local minima. Verification shows that compared to the traditional BP neural network, the predicted deformation value corresponding to the optimal welding sequence decreased by approximately 21.07%.

(2) Multiple welding numerical simulations of the double-T thin plate were conducted using simulation software, and various welding sequences and corresponding deformation values were obtained. The results were organized into a dataset, which was experimentally verified for accuracy. Finally, both traditional BP neural network and SA-BP neural network models were used to validate the dataset. The traditional BP model was trapped in a local optimum, whereas the SA-BP model showed an MSE reduction of 0.00096 compared to the traditional BP neural network model. The results demonstrated higher stability and accuracy in detection.

(3) This study has achieved notable results but still has some limitations. First, the research primarily focuses on relatively simple double T-shaped thin plate structures, whereas more complex welding structures (such as multi-stiffened plates or curved plates) in real-world production may involve more variables and greater optimization challenges. Second, due to constraints on time and computational resources, the dataset used in this study is limited to 500 welding sequences, which may not fully capture all possible deformation characteristics. Additionally, while the Simulated Annealing algorithm was employed to optimize the BP neural network, the selection and tuning of algorithm parameters (e.g., initial temperature, cooling rate) were not thoroughly explored, potentially impacting the model's optimal performance. Lastly, the experimental validation was conducted under controlled conditions, which

might not fully account for complex factors in real-world production environments, such as material microstructures and ambient temperature variations, potentially limiting the model's direct applicability in industrial settings.

(4) In the future, this study could be extended in several directions to enhance its applicability and effectiveness. First, the proposed method can be applied to more complex welding structures, such as multi-stiffened plates and curved panels, to verify its robustness and generalizability. Second, larger and more diverse datasets could be generated using high-performance computing resources, allowing for better coverage of complex welding scenarios and improving model accuracy. Third, further research could focus on optimizing the parameters of the Simulated Annealing algorithm and conducting sensitivity analyses to identify the optimal settings for enhanced model performance. Additionally, multi-objective optimization approaches could be explored by incorporating other factors such as residual stress, production cost, and welding efficiency, providing a more comprehensive solution for industrial applications. Finally, practical experiments in real-world production environments should be conducted to validate the model's effectiveness, assess its industrial feasibility, and refine it based on feedback from actual implementation.

## Funding

This research is funded by the Shipbuilding Industry Technology Capability Enhancement Special Program (Grant No.: QT1451-0415043).

## Data Availability

The data used to support the research findings are available from the corresponding author upon request.

## Conflicts of Interest

The authors declare no conflict of interest.

## References

- [1] H. T. Ding, W. Y. Zhang, Z. Y. Zhang, D. D. Yin, W. T. He, and D. Xie, "Influence of welding sequences and boundary conditions on residual stress and residual deformation in DH36 steel T-joint fillet welds," *Thin-Walled Struct.*, vol. 204, p. 112337, 2024. <https://doi.org/10.1016/j.tws.2024.112337>
- [2] D. Deng and H. Murakawa, "FEM prediction of buckling distortion induced by welding in thin plate panel structures," *Comput. Mater. Sci.*, vol. 43, no. 4, pp. 591–607, 2008. <https://doi.org/10.1016/j.commatsci.2008.01.003>
- [3] B. Q. Chen and C. G. Soares, "Experimental and numerical investigation on welding simulation of long stiffened steel plate specimen," *Mar. Struct.*, vol. 75, p. 102824, 2021. <https://doi.org/10.1016/j.marstruc.2020.102824>
- [4] M. Ghafouri, A. Ahola, J. Ahn, and T. Björk, "Numerical and experimental investigations on the welding residual stresses and distortions of the short fillet welds in high strength steel plates," *Eng. Struct.*, vol. 260, p. 114269, 2022. <https://doi.org/10.1016/j.engstruct.2022.114269>
- [5] F. G. Lu, D. A. Deng, Y. Q. Wang, and C. D. Shao, "Application and development of numerical simulation technology in laser welding process," *Trans. China Weld. Inst.*, vol. 43, no. 8, pp. 87–94, 2022. <https://doi.org/10.12073/j.hjxb.20220430001>
- [6] W. M. Zhao, W. Jiang, H. J. Zhang, B. Han, H. C. Jin, and Q. Gao, "3D finite element analysis and optimization of welding residual stress in the girth joints of X80 steel pipeline," *J. Manuf. Process.*, vol. 66, pp. 166–178, 2021. <https://doi.org/10.1016/j.jmapro.2021.04.009>
- [7] N. Azad, M. Iranmanesh, and A. Rahmati Darvazi, "A study on the effect of welding sequence on welding distortion in ship deck structure," *Ships Offshore Struct.*, vol. 15, no. 4, pp. 355–367, 2019. <https://doi.org/10.1080/17445302.2019.1619898>
- [8] J. M. Sun and K. Dilger, "Influence of welding sequence and external restraint on buckling distortion in thin-plate arc-welded joints," *J. Adv. Join. Process.*, vol. 8, p. 100157, 2023. <https://doi.org/10.1016/j.jajp.2023.100157>
- [9] X. X. Zhao, P. Zhang, J. G. Li, T. Ma, C. Y. Miao, R. Y. Zhang, S. Y. Wu, Y. L. Zhao, J. L. Zhu, and X. Jiao, "Cover plate welding sequence and shape rationality simulation analysis on wall cracks of stainless steel spent fuel pool," *Prog. Nucl. Energy*, vol. 154, p. 104481, 2022. <https://doi.org/10.1016/j.pnucene.2022.104481>
- [10] V. Emelianov, A. Zhilenkov, S. Chernyi, A. Zinchenko, and E. Zinchenko, "Application of artificial intelligence technologies in metallographic analysis for quality assessment in the shipbuilding industry," *Heliyon*, vol. 8, no. 8, p. e10002, 2022. <https://doi.org/10.1016/j.heliyon.2022.e10002>
- [11] G. Turichin, M. Kuznetsov, I. Tsibulskiy, and A. Firsova, "Hybrid laser-arc welding of the high-strength shipbuilding steels: Equipment and technology," *Phys. Procedia*, vol. 89, pp. 156–163, 2017. <https://doi.org/10.1016/j.phpro.2017.08.005>

- [12] M. S. Choobi, M. Haghpanahi, and M. Sedighi, "Prediction of welding-induced angular distortions in thin butt-welded plates using artificial neural networks," *Comput. Mater. Sci.*, vol. 62, pp. 152–159, 2012. <https://doi.org/10.1016/j.commatsci.2012.05.032>
- [13] C. Sun and C. Zhen, "End-to-end deep learning method to reconstruct full-field stress distribution for ship hull structure with stress concentrations," *Ocean Eng.*, vol. 313, no. 1, p. 119431, 2024. <https://doi.org/10.1016/j.oceaneng.2024.119431>
- [14] Y. Su, W. Y. Li, J. J. Shen, L. Bergmann, J. F. dos Santos, B. Klusemann, and A. Vairis, "Comparing the fatigue performance of Ti-4Al-0.005 B titanium alloy T-joints, welded via different friction stir welding sequences," *Mater. Sci. Eng. A*, vol. 859, p. 144227, 2022. <https://doi.org/10.1016/j.msea.2022.144227>
- [15] W. Fricke, A. von Lilienfeld-Toal, and H. Paetzold, "Fatigue strength investigations of welded details of stiffened plate structures in steel ships," *Int. J. Fatigue*, vol. 34, no. 1, pp. 17–26, 2012. <https://doi.org/10.1016/j.ijfatigue.2011.01.021>
- [16] Z. Li, Y. J. Guo, H. Y. Dong, F. Yuan, H. L. Wu, H. Xu, and Y. L. Ke, "Numerical prediction and control of deformation and residual stress in double-sided arc welding of large pressure hull," *Measurement*, vol. 242, p. 115955, 2025. <https://doi.org/10.1016/j.measurement.2024.115955>
- [17] H. D. Seo and J. M. Lee, "A new welding distortion analysis method considering inherent deformation-based tendon force estimation," *Int. J. Nav. Archit. Ocean Eng.*, vol. 17, p. 100640, 2024. <https://doi.org/10.1016/j.ijnaoe.2024.100640>
- [18] J. Goldak, A. Chakravarti, and M. Bibby, "A new finite element model for welding heat sources," *Metall. Trans. B*, vol. 15, pp. 299–305, 1984. <https://doi.org/10.1007/BF02667333>
- [19] H. J. Zhang, Y. Wang, T. Han, L. L. Bao, Q. Wu, and S. W. Gu, "Numerical and experimental investigation of the formation mechanism and the distribution of the welding residual stress induced by the hybrid laser arc welding of AH36 steel in a butt joint configuration," *J. Manuf. Process.*, vol. 51, pp. 95–108, 2020. <https://doi.org/10.1016/j.jmapro.2020.01.008>
- [20] M. Son and H. Ki, "Deep-learning model for predicting hardness and phase distributions from two cross-sectional temperature distribution images in laser heat treatment of AH36 steel," *J. Mater. Res. Technol.*, vol. 27, pp. 718–732, 2023. <https://doi.org/10.1016/j.jmrt.2023.09.300>
- [21] J. B. Feng, X. C. Yong, P. L. Zhang, Z. F. Li, L. X. Song, X. Z. Su, J. X. Li, and Z. S. Yu, "Research on the dynamic process and defect formation in laser-arc hybrid welding of 12-mm thick AH36 steel," *Int. J. Adv. Manuf. Technol.*, vol. 135, pp. 1–17, 2024. <https://doi.org/10.1007/s00170-024-14515-6>
- [22] J. M. Sun, J. Hensel, J. Klassen, T. Nitschke-Pagel, and K. Dilger, "Solid-state phase transformation and strain hardening on the residual stresses in S355 steel weldments," *J. Mater. Process. Technol.*, vol. 265, pp. 173–184, 2019. <https://doi.org/10.1016/j.jmatprotec.2018.10.018>
- [23] H. Y. Yang, X. T. Li, W. H. Qiang, Y. H. Zhao, W. Zhang, and C. Tang, "A network traffic forecasting method based on SA optimized ARIMA–BP neural network," *Comput. Netw.*, vol. 193, p. 108102, 2021. <https://doi.org/10.1016/j.comnet.2021.108102>
- [24] W. Dai, "A method of multiobjective synthetic evaluation based on artificial neural networks and its applications," *Syst. Eng.-Theory Pract.*, vol. 5, pp. 29–34, 1999.
- [25] C. Y. Lin, M. I. Sam, Y. C. Tsai, and H. H. Lin, "Critical neurons: Optimized visual recognition in a neuronal network," *arXiv Preprint*, 2022. <https://doi.org/10.48550/arXiv.2211.15278>
- [26] A. Saffaran, M. Azadi Moghaddam, and F. Kolahan, "Optimization of backpropagation neural network-based models in EDM process using particle swarm optimization and simulated annealing algorithms," *J. Braz. Soc. Mech. Sci. Eng.*, vol. 42, no. 1, p. 73, 2020. <https://doi.org/10.1007/s40430-019-2149-1>